LASER & PHOTONICS REVIEWS
www.lpr-journal.org

Fast and Efficient Inverse Design Framework for Multifunctional Metalenses

Xixian Zu, Xiaoyu Sun, Wei Yan, Wei E. I. Sha, and Min Qiu**

Over the past years, nanostructured metalenses with thin form factors have been extensively studied for their potential in consumer and industrial applications. Despite significant advancements, current metalenses struggle to achieve high numerical aperture (NA), manufacturable structures, broad working bandwidth, and extended depth of focus (DOF) simultaneously. This paper introduces a comprehensive inverse design framework that facilitates the rapid development of polarization-insensitive 3D metalenses, effective in both frequency and spatial domains. The framework employs shape-constrained topology optimization to define horizontal ring profiles, along with discrete particle swarm optimization to manage discretized ring heights. Two immersed silicon carbide metalenses are demonstrated to showcase this framework's capability, providing near-unity NAs for enhanced photon collection. The first design is an extended DOF metalens, exhibiting a DOF over four times the light wavelength and achieving a maximum diffraction efficiency of 23%, close to the theoretical limit. The second design achieves broadband achromaticity, suppressing chromatic aberrations across a wide 300 nm bandwidth (850–1150 nm) while maintaining an average diffraction efficiency of 10%. This methodology serves as a valuable tool for deploying functional metalenses with implications for nanophotonics, quantum optics, and quantum nanotechnology.

1. Introduction

Advancements in metalenses have demonstrated exceptional capabilities in diverse applications such as imaging, microscopy, spectroscopy, and lithography.[1–5] Specifically, due to their superior focusing and resolving abilities, metalenses with high numerical aperture (NA) play a crucial role in optical applications that demand high-resolution or wide-angle light-gathering capabilities, such as single-photon extraction from quantum emitters.[6–9]

Traditionally, the intuitive "unit cell" approach has pioneered initial metalens designs, whereby focusing is attained by assembling collections of wavelength-scale meta-atoms.[10] The required phase profile of the metalens is fulfilled by mapping geometric variations in meta-atoms. However, the simplifications inherent in this approach, including discrete phase sampling, local periodicity approximation, and normal-incidence response, imply that the responses and interactions of meta-atoms are almost impossible to accurately model.[11–13] This inaccuracy grows in the case of high-NA focusing, wherein the amplitude and phase of the outgoing field undergo rapid variations. Such a method is difficult to a design high-efficiency, high-NA focusing lens, even for a single-wavelength operation.

More recently, inverse design, employing algorithmic techniques to discover optical structures based on desired functional attributes, has reshaped the landscape of nanophotonic design.[14–16] Among these techniques, adjoint-based topology optimization (TO) stands out for its notable advantages in computational efficiency.[17] TO leverages the Born approximation and Lorentz reciprocity to rapidly compute gradients for all voxels within the design domain, by performing only two electromagnetic simulations per iteration. This enables the rapid adjustment of the dielectric constant across all device voxels, and, generally, after hundreds of iterations, the design converges to a local optimum.[18,19] Preliminary studies have applied TO to the development of metalenses, focusing on optimizing either in-plane or out-of-plane material distribution.[20–24] However, metalenses derived from TO tend to exhibit pixel-by-pixel variations of meta-atoms, even at deep subwavelength scales, leading to extremely sensitive and unpredictable alterations of electromagnetic scattering responses.[25] Additionally, the limited degrees of freedom (DoFs) of in-plane optimization present challenges for integrating multiple functionalities across both frequency and spatial domains. In contrast, metalenses optimized by out-of-plane TO tend to have numerous height levels which are

X. Zu, X. Sun, W. E. I. Sha
College of Information Science and Electronic Engineering
Zhejiang University
Hangzhou, Zhejiang 310027, China
E-mail: weisha@zju.edu.cn
X. Zu, X. Sun, W. Yan, M. Qiu
Zhejiang Key Laboratory of 3D Micro/Nano Fabrication and Characterization
School of Engineering
Westlake University
Hangzhou, Zhejiang 310030, China
E-mail: qiumin@westlake.edu.cn
M. Qiu
Westlake Institute for Optoelectronics
Fuyang, Hangzhou, Zhejiang 311421, China
X. Zu, X. Sun, W. Yan, M. Qiu
Institute of Advanced Technology
Westlake Institute for Advanced Study
18 Shilongshan Road, Hangzhou, Zhejiang 310024, China

DOI: 10.1002/lpor.202400886

exceedingly difficult to fabricate. Typically, these metalenses can only be produced using additive methods such as two-photon polymerization lithography, which are limited to low-refractive index materials that provide weak optical control due to insufficient light confinement. More layers are required to enhance performance, introducing additional complexity in simulation and fabrication.[26] Both types of metalenses necessitate full-wave simulations throughout the design process, resulting in significant CPU memory and time expenses and severely restricting the size of the metalenses.

In the absence of fast and accurate methods for the rapid attainment of scalable and manufacturable multifunctional metalenses with high efficiency, we introduce a hybrid inverse design framework that synergistically integrates shape-constrained topology optimization (SCTO) with discrete particle swarm optimization (DPSO) to enable cross-dimensional cooperative optimization. SCTO determines the horizontal ring profile, and DPSO regulates the discretized heights of rings (fewer than 4 height levels in the demonstrations of this work). This approach offers abundant DoFs while maintaining features conducive to device fabrication. It strikes a balance between design flexibility, computational efficiency, and fabrication precision.

To demonstrate the capabilities of our design framework, we apply it to inversely design two distinct immersed silicon carbide (SiC) metalenses, addressing the challenges of extending depth of focus (DOF) and minimizing chromatic aberration. SiC is a vital platform for realizing spin-based quantum technologies, harboring numerous optically addressable defects known as color centers[27] with extremely high brightness and long spin coherence time.[28–30] Immersed SiC metalenses are potentially revolutionary candidates for enhancing photon collection efficiency.[6,7,31] Achieving longitudinal optical field modulation is crucial for extracting color centers with implanting spatial uncertainty. Nonetheless, developing high-efficiency, high-NA metalens with an extended DOF remains a significant challenge.[32] In this work, we present and experimentally demonstrate an extended DOF metalens with a near-unity NA, achieving a measured maximum diffraction efficiency of 23%, approaching the theoretical limit calculated by vector diffraction theory.[33] Additionally, we successfully design an achromatic metalens exhibiting a significantly expanded group delay range across a wide bandwidth of 850–1150 nm, featuring an ultra-high NA of 0.984. To date, no work has demonstrated such a broad bandwidth at such a high NA. These metalens can effectively extract photoluminescence (PL) from the three most prevalent types of SiC color centers: the silicon vacancy V_{Si}^{-}, the divacancy $V_{Si}V_{C}^{0}$ and the chromium ion Cr^{4+}. One noteworthy point to highlight is the adaptability of this inverse design framework, which lends itself seamlessly to the expansion into scalable metalenses utilizing alternative material platforms tailored to specific functionalities. We anticipate that these inverse-designed devices will facilitate the scalable nanophotonic integration of single-photon emitters, rapid characterization of new quantum emitters, efficient sensing, and heralded entanglement schemes.

2. Hybrid Inverse Design Framework

As shown in **Figure** 1b, a hybrid inverse design framework that combines local optimization and global optimization techniques is introduced. This framework provides sufficient design DoFs while maintaining device fabrication-friendly features in designing the multifunctional metalens shown in Figure 1a. In the local optimization solver section, SCTO is used to determine the horizontal material profile. TO leveraging the adjoint variables method can modify the dielectric constant at all device voxels in a given optimization iteration with just two full-wave simulations. Usually, the optimization process converges to a local optimum within hundreds of iterations based on the desired figure of merit (FoM). We arrange the voxels in the design domain into concentric rings. Refining the design mesh as concentric circular rings offers several advantages. First, it imposes a shape constraint to avoid pixel-by-pixel variation in geometry, thereby improving structural robustness. Second, the device is naturally polarization-insensitive due to its continuous rotational symmetry. Therefore, a 2D Helmholtz-type partial differential equation can be used to approximately model interactions between light and structures under a linear incident electric field, effectively reducing the computational complexity of electromagnetic calculations.

To bridge the disparity between scalar and vector diffraction theory regarding phenomena such as focal spot shift and efficiency variations, and to enhance design flexibility by introducing additional DoFs such as the height of rings for further device optimization, we conduct another global heuristic optimization (e.g., DPSO[34]), which is well-suited for problems involving a small number of DoFs. The optimal index profile from SCTO is subsequently passed to the global optimization solver, where DPSO is used to further improve the FoM with a fixed index profile but varying heights of the dielectric rings. Again, taking advantage of the continuous rotational symmetry of the structure, we perform 2D axisymmetric simulations rather than 3D to drastically cut down on computational time and resources while maintaining accuracy.[35] This framework expedites the design procedure by exploiting the essence of polarization-insensitive focus and is capable of capturing the individual and collective behaviors of concentric rings.

3. Extended Depth-of-Focus Metalens

To showcase the capability of our framework, we design an immersed SiC metalens with extended DOF, which can be utilized to extract PL emitted from SiC color centers with spatial implanting uncertainty. The metalens has a diameter of 26 μm and the target operating wavelength is 1064 nm. The FoM is defined as:

$$\Phi = \max_{r \in R} \left\{ \min \left(|\mathbf{E}(\xi, r)|^2 \right) \right\} \tag{1}$$

$$\text{s.t. } \varepsilon_r(\xi) = \varepsilon_{r,air} + \xi \cdot \left(\varepsilon_{r,SiC} - \varepsilon_{r,air} \right) \tag{2}$$

$$0 \le \xi \le 1 \tag{3}$$

This formulation aims to maximize the minimum intensity at various focal points along the focal axis. Here, ξ represents the density field that defines the metalens. The values of ξ range from 0 to 1, where 0 corresponds to air and 1 corresponds to SiC. The function $\varepsilon_r(\xi)$ describes the position-dependent effective permittivity profile used in the inverse design process. R is a set of

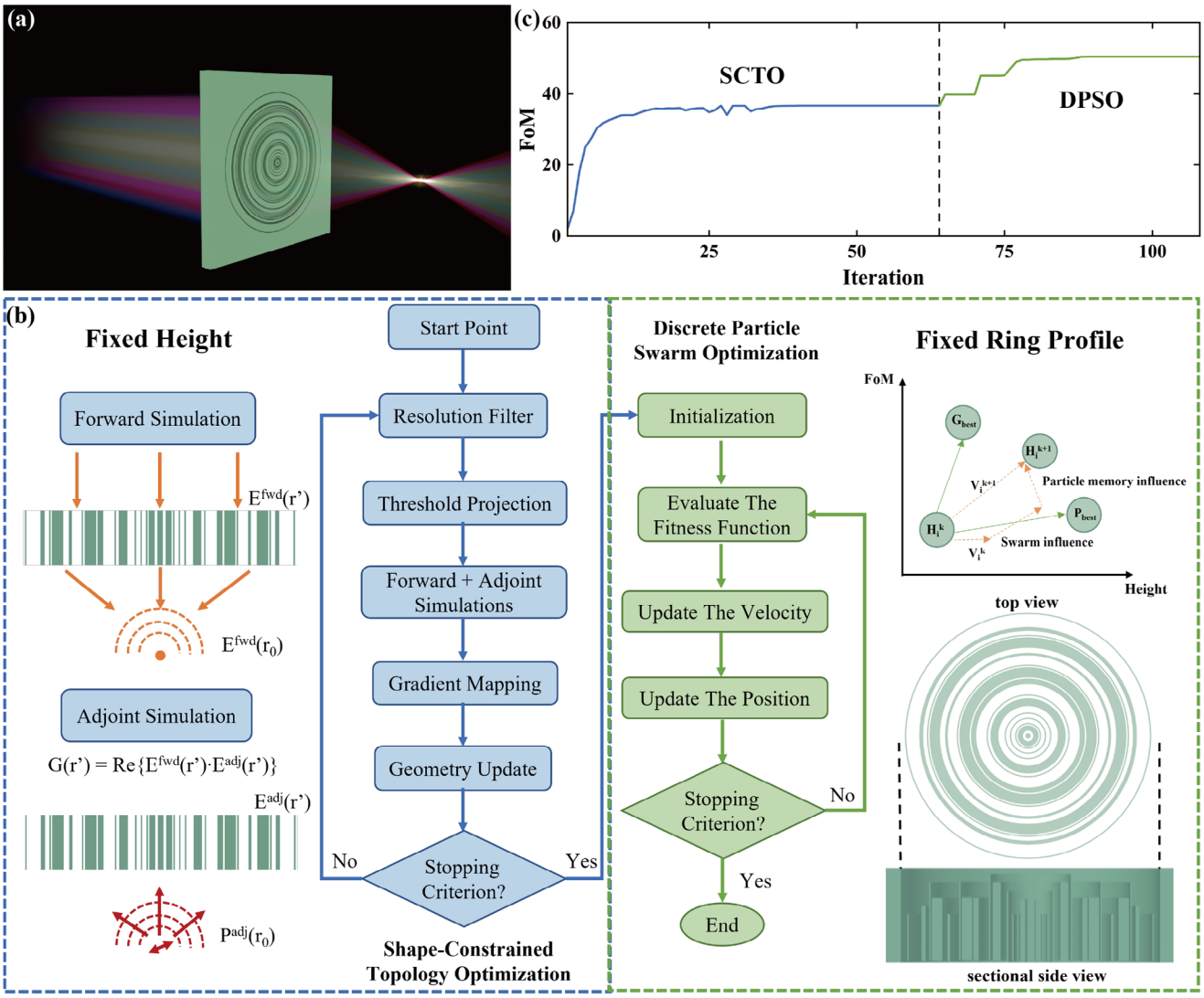

Figure 1. Hybrid inverse design framework. a) Schematic of the multifunctional metalens. b) Algorithm flowchart of cooperative optimization. The local optimizer is shape-constrained topology optimization (SCTO) to determine the horizontal lens index profile with a fixed height. The global optimizer is discrete particle swarm optimization (DPSO) to determine the height variation based on the index profile from SCTO. c) FoM evolution over hybrid optimization process for the extended DOF metalens. The local optimization solver (SCTO) takes 64 iterations and the global optimization solver (DPSO) takes 44 iterations. By incorporating the global optimization solver, FoM increases by 37.6% from 36.7 to 50.5.

target points along the focal axis, and $|\mathbf{E}(\xi, r)|^2$ denotes the electric field intensity at the focal point r for a metalens defined by the density field ξ. To better control the depth of focus, the focal points should be linearly spaced along the optical axis to cover a desired DOF with sufficiently small spacing. In this particular scenario, we specifically sample four spatial points, ranging from 1 to 4 μm above the upper surface of the metalens, with increments of 1 μm. The optical constant of SiC is measured by an ellipsometer (J.A. Woollam, RC2 XI+) and can be found in Note S1 (Supporting Information). Starting from the initial structure, we achieve the local optimum through iterative updating. In each generation, the structure is blurred, filtered, and binarized, and the threshold sharpness increases with the iterations. Therefore, each pixel in the design area is represented by a value that varies continuously from 0 to 1 during the optimization process and will eventually become binary, with 0 representing air and 1 representing SiC. The pixel size in the radial direction is set to 50 nm, considering the fabrication tolerance. As shown in Figure 1c, the local optimization solver (SCTO) takes 64 iterations, and the global optimization solver (DPSO) takes 44 iterations to converge. By incorporating the global optimization solver, the FoM increases by 37.6%, from 36.7 to 50.5. The detailed structural parameters can be found in Note S2 (Supporting Information), consisting of 35 concentric rings with 4 height levels ranging from 0.2 to 0.5 μm, which is relatively easier to fabricate.

Figure 2a presents the simulated normalized electric field intensity distribution of the xz cross section optimized by SCTO

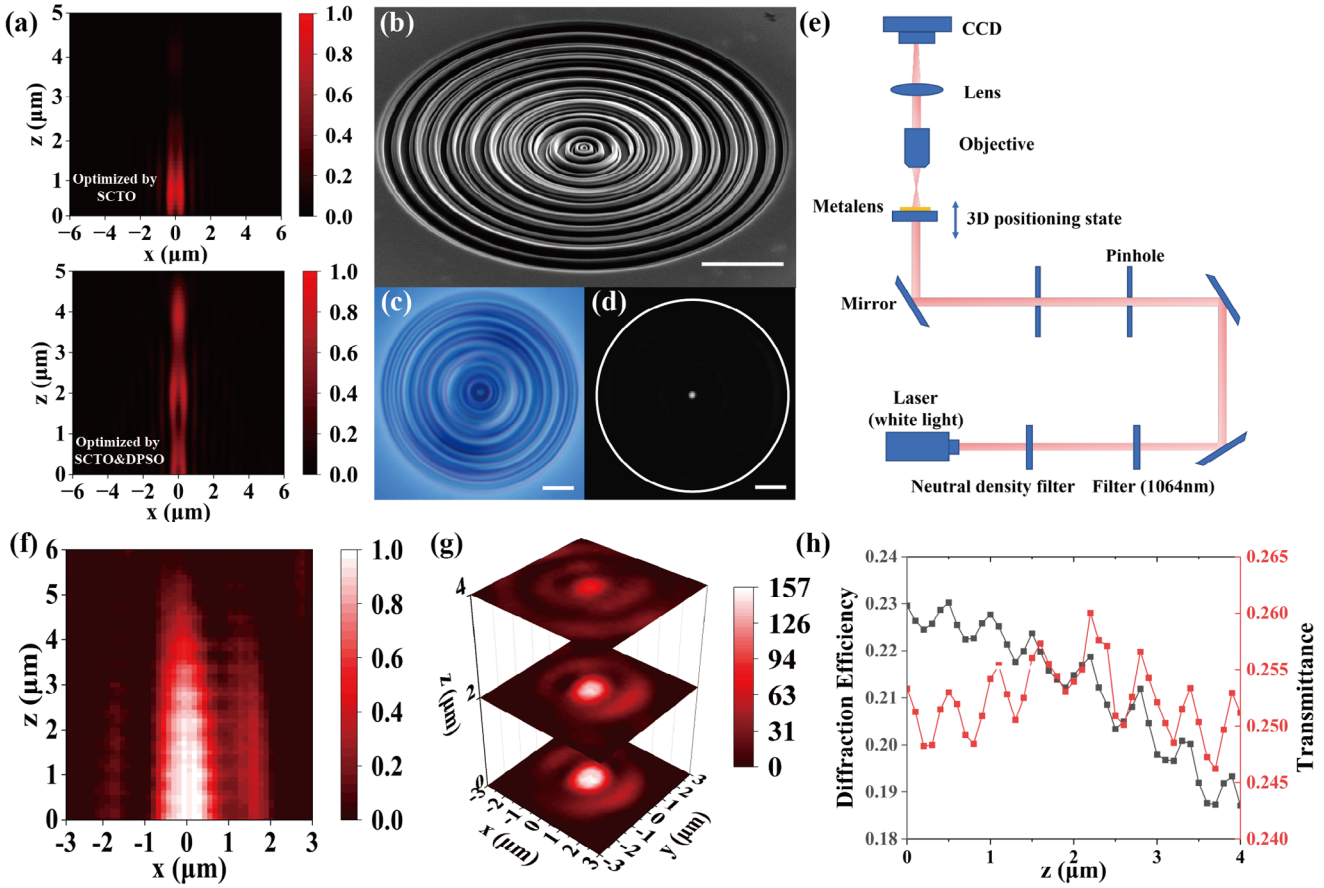

Figure 2. Fabrication and optical characterization of extended-depth-of-focus metalens. a) Normalized simulated electric field intensity distribution at xz cross section. Top: optimal result from SCTO; Down: optimal result from SCTO&DPSO. b) SEM image of the device. c) Bright-field optical microscope image of the upper surface of the metalens. d) Dark-field optical microscope image of the focal plane. The white ring indicates the effective aperture of the metalens. All scale bars denote 5 μm. e) Schematic of the measurement setup. f) Normalized measured light intensity distribution at xz cross section. g) Measured 3D stacked optical intensity images, shown at a step of 2 μm. h) Measured transmittance and diffraction efficiency of the metalens.

(top) and jointly optimized by SCTO and DPSO (bottom). In Figure 2a, the positions of the maximum intensity are away from the optical axis along the x-axis. The split of the bimodal focus is attributed to the depolarization effect[36] for near-unity aperture lens. This occurs when the longitudinal z component of the electric field interferes in the focal region and has comparable intensity to the x component. Here, the DOF is defined as the position where the electric field intensity along the z-axis is greater than 80% of the maximum.[32] The DOF is greatly improved up to 4.11 μm, which is 6 times higher than that of the sole SCTO optimization.

The pristine sample is a commercially available high-purity semi-insulating 4H-SiC wafer. We fabricate the immersed metalens using a top-down focused ion-beam milling system with Gallium ions (Thermo Scientific Helios 5 UX) with an acceleration voltage of 30 kV and a beam current of 90 pA (corresponding spot size of 20.4 nm). Figure 2b,c shows the scanning electron microscope (SEM) image and the optical image of the fabricated device. We employ a lab-built transmission setup in Figure 2e to characterize the focusing performance of the metalens. A CW laser beam is modulated by a filter to generate a 1064 nm source and is incident on the metalens. A 100x objective (SOPTOP LM-PlanFL, NA = 0.8) is used to collect the light modulated by the sample and image information to a CMOS camera (Thorlabs UI-3240CP-NIR-GL-TL). The magnification of the microscope was found by imaging and calibrating a feature point through the movement of the stage. Figure 2d depicts the optical image of the focal plane in a dark field. A distinct and bright focal spot is clearly visible. To quantify the light focusing by the metalens, the focal spot is analyzed by capturing 100 images taken at 0.1 μm step from the top of the metalens (z = 0). The measured light intensity distribution at the xz cross section is normalized (Figure 2f) to compare with the simulation result (Figure 2a). It is clear that the extension of the DOF has been successfully achieved, which is also consistent with the simulation results. Obvious ripples can be observed in Figure 2g, which is common for high NA metalens.[20] The measured full width at half maximum (FWHM) is 1.625 μm, larger than the simulated value of 0.97 μm. The expanded focal spots are attributed to the redeposition effect and sputter yields. These effects are inevitable in the FIB milling of 3D microstructures.[37] Moreover, the discrepancy in NA between the adopted objective and the metalens contributes to the collected attenuation of edge light, further exacerbating the energy dispersion of the metalens. Despite potential profile inaccuracies

Table 1. Summary of performance metrics for broadband achromatic metalenses.

Diameter [μm]	Relative bandwidth	NA	Highest focusing efficiency	Polarization	Material	Ref.
100	27.6%	0.2	32.01%	Insensitive	IP-L 780 polymer	[40]
100	31.58%	0.24	50%	Insensitive	Si	[41]
30	42.42%	0.24	77.1%	Insensitive	TiO_2	[42]
20	116.3%	0.27	60%	Insensitive	IP-DIP photoresist	[43]
20	66.67%	0.7	22.1%	Insensitive	IP-DIP resin	[26]
32	7.84%	0.81	27.5%	Circular	Si	[44]
26	30%	0.984	13.6%	Insensitive	SiC	This work

stemming from structural adherence and measurement errors, the experimental outcomes align with expectations, affirming the remarkable resilience of the proposed design. We then investigate the efficiency of the metalens, as shown in Figure 2h. The transmission efficiency represents the proportion of the energy transmitted through the metalens to the incident energy. The diffraction efficiency is calculated as the ratio between the optical intensity in an area with a diameter of three times the FWHM at the focal plane and the transmitted light intensity. As the propagation distance increases, the diffraction efficiency declines, with the maximum reaching 23%, approaching the theoretical limit calculated by vector diffraction theory.[33] The average transmittance is 25.24%, which is relatively low due to intrinsic losses and the high refractive index of the material. In comparison to a bare substrate with a transmittance of 27%, the metalens exhibit a relative transmittance of 93.48%.

4. Broadband Achromatic Metalens

SiC has proven to be a versatile host to optically addressable, long-lived spin cubits, including two most well-studied color centers: the silicon vacancy V_{Si}^{-} (zero phonon line (ZPL): 862–917 nm) and the divacancy $V_{Si}V_{C}^{0}$ (ZPL: 1078–1132 nm). Other defects such as the chromium ion Cr^{4+} (ZPL: 1042, 1070 nm) are emerging to offer new functionalities.[38] In complex SiC polytypes like 4H and 5H, multiple inequivalent lattice sites coexist within a crystal unit cell. Consequently, each defect can be a family of several defect types with similar but not identical properties.[39] Achromatic metalenses can be utilized to extract photons emitted by a series of color centers from the high-index substrate for multiple further operations.

Up to now, extensive research has been undertaken to design broadband achromatic metalenses. **Table 1** summarizes the important metrics (diameter, relative bandwidth, NA, highest focusing efficiency, polarization sensitivity, and material) of different achromatic metalenses in previous works. At present, most broadband achromatic metalenses are characterized by either low NA or narrow bandwidth. However, constraints in the range of group delay provided by the meta-units result in a significant decrease in NA that obscures high-resolution imaging, making them unable to fully meet the demanding requirements of quantum optics. Moreover, it remains a huge challenge to achieve high NA and a large operational bandwidth simultaneously due to the finite group delay range provided by meta-units. Therefore, designing a high NA and polarization-insensitive broadband achromatic metalens remains a tricky problem.

We Utilize the Introduced Framework to Put Forward the High NA and Polaization-Insensitive Broadband Achromatic METALENS, with the FoM Identified as

$$\Phi = \max_{\omega \in \Omega} \left\{ \min \left(|\mathbf{E}(\xi, \omega)|^2 \right) \right\} \tag{4}$$

$$\text{s.t. } \varepsilon_r(\xi) = \varepsilon_{r,\text{air}} + \xi \cdot \left(\varepsilon_{r,\text{SiC}} - \varepsilon_{r,\text{air}} \right) \tag{5}$$

$$0 \le \xi \le 1 \tag{6}$$

This formulation aims to maximize the minimum intensity across a frequency band. Here, ξ represents the density field that defines the metalens. The values of ξ range from 0 to 1, where 0 corresponds to air and 1 corresponds to SiC. The function $\varepsilon_r(\xi)$ describes the position-dependent effective permittivity profile used in the inverse design process. Ω is a set of discrete frequencies of interest, and $|\mathbf{E}(\xi, \omega)|^2$ denotes the electric field intensity at a particular frequency ω for a metalens defined by the density field ξ.

The designed achromatic metalens are shown in **Figure 3**a, whose detailed structural parameters can be found in Note S3 (Supporting Information). The metalens are featured with 3 height levels, varying from 0.8 to 1.2 μm with a step size of 0.2 μm. Figure 3b shows the exact focal length at any given wavelength ranging from 850 to 1150 nm, corresponding to the z-coordinate possessing the highest intensity value. This bandwidth effectively encompasses the specified color centers by maintaining a consistent focal length throughout the entire range, with a mean square error in deviation of 0.0934 μm. The negligible variation in focal length is further illustrated by examining the point spread function at a target focal length of 1.8 μm, where no defocusing effects are observed. To confirm the achromatic performance of the designed metalens, the focal lengths at various wavelengths are evaluated by analyzing the intensity profiles along the z-axis of a continuous wave incident light beam, as depicted in Figure 3d. The distribution of lens intensity demonstrates that chromatic aberrations are markedly diminished across the entire 300 nm bandwidth, with an observable focal length variation of no consequence. In fact, the outstanding suppression of chromatic aberrations suggests that the focal spot would maintain its profile for an appreciable increase of the characterization spectrum. Furthermore, it is often observed that parasitic focal spots are present, typically due to arbitrary design strategies, suggesting that the

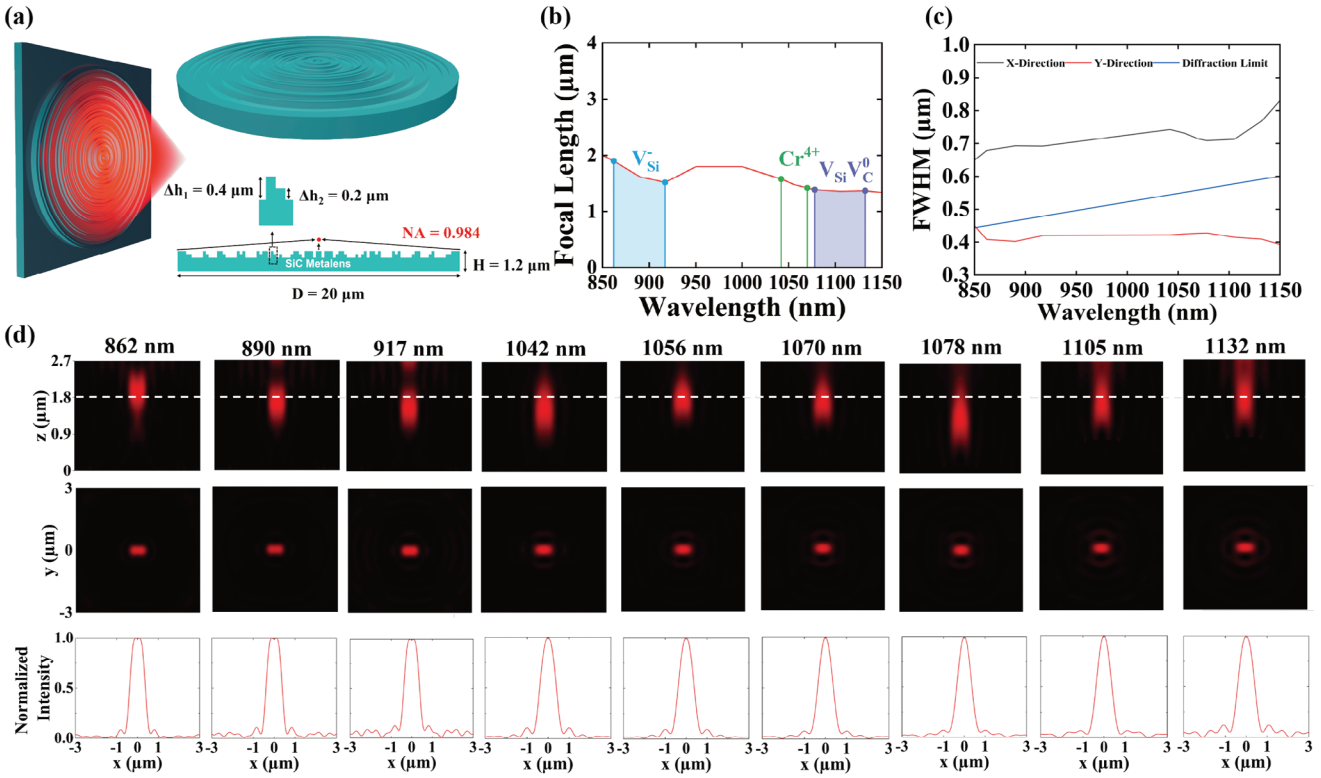

Figure 3. Achromatic broadband metalens for extracting PL from different types of SiC color centers. a) Schematic diagram of the metalens. b,c) Simulated focal length and FWHM for broadband metalens. d) Simulated intensity distributions of x-z cross-section and x-y focal plane for 9 selected wavelengths applicable to three different types of color centers.

metalens do not precisely focus the incoming light beam. However, our methodology successfully addresses these issues. In this instance, as depicted in Figure 3c, the FWHM of the focal spots varies distinctly between the x- and y-direction due to the extremely high NA of 0.984 and x-polarized incident light. For the ultrahigh-NA metalens, the FWHM along the y-direction is considerably narrower compared to the x-direction, resulting in a super-diffraction focusing effect in the y-direction.

5. Conclusion

To summarize, we have presented an approach for designing polarization-insensitive focusing devices both in the frequency and spatial domain using a hybrid inverse design framework. This framework combines local optimization techniques, such as SCTO, with global optimization methods like DPSO. The SCTO design process involves refining the mesh into concentric circular rings to improve structure robustness and insensitivity to polarization. Incorporating DPSO to increase design DoFs further enhances the FoM by 37.6%. Additionally, this framework utilizes scalar diffraction theory and 2D axisymmetric simulations to expedite computational processes while maintaining accuracy. The capacity of this approach is verified by two superior types of metalenses—extended-depth-of-focus and broadband achromatic—that outperform most existing designs. The design of the metalens is both adaptable and scalable, making it suitable not only for SiC but also for various other material platforms. This represents crucial progress in the creation of compact, high-efficiency focusing devices and has widespread implications for nanophotonics, quantum optics, and quantum nanotechnology.

Supporting Information

Supporting Information is available from the Wiley Online Library or from the author.

Acknowledgements

The authors express their gratitude to the Westlake Centre for Micro/Nano Fabrication and the Westlake Instrumentation and Service Center for Physical Sciences for their facility support and technical assistance. Special funding for Talent Introduction of the Qiu Min Laboratory of Westlake University (103166021801).

Conflict of Interest

The authors declare no conflict of interest.

Author Contributions

Min Qiu, Wei E.I. Sha, and Wei Yan led the research project. Xixian Zu is responsible for the design, fabrication and characterization of the devices. Xiaoyu Sun and Xixian Zu conducted the optical measurements. All authors contributed to the discussion and writing of the manuscript.

Data Availability Statement

The data that support the findings of this study are available in the supplementary material of this article.

Keywords

broadband achromatic, cooperative optimization, extended depth-of-focus, inverse design, metalenses

Received: June 14, 2024
Revised: September 1, 2024
Published online: October 10, 2024

[1] Y. Li, S. Chen, H. Liang, X. Ren, L. Luo, Y. Ling, S. Liu, Y. Su, S. T. Wu, *PhotoniX* **2022**, *3*, 29.
[2] S. Uenoyama, Y.u Takiguchi, K. Takahashi, K. Hirose, H. Terada, A. Watanabe, *Opt. Lett.* **2020**, *45*, 6218.
[3] P. Lin, W. T. Chen, K. M. A. Yousef, J. Marchioni, A. Zhu, F. Capasso, J. X. Cheng, *APL Photonics* **2021**, *6*, 096107.
[4] W. Hadibrata, H. Wei, S. Krishnaswamy, K. Aydin, *Nano Lett.* **2021**, *21*, 2422.
[5] X. Luo, *ACS Photonics* **2023**, *10*, 2116.
[6] R. Paniagua-Domínguez, Y. F. Yu, E. Khaidarov, S. Choi, V. Leong, R. M. Bakker, X. Liang, Y. H. Fu, V. Valuckas, L. A. Krivitsky, A. I. Kuznetsov, *Nano Lett.* **2018**, *18*, 2124.
[7] T. Y. Huang, R. R. Grote, S. A. Mann, D. A. Hopper, A. L. Exarhos, G. G. Lopez, A. R. Klein, E. C. Garnett, L. C. Bassett, *Nat. Commun.* **2019**, *10*, 2392.
[8] M. Meem, S. Banerji, C. Pies, T. Oberbiermann, A. Majumder, B. Sensale-Rodriguez, R. Menon, *Optica* **2020**, *7*, 252.
[9] Y. Ha, Y. Luo, M. Pu, F. Zhang, Q. He, J. Jin, M. Xu, Y. Guo, X. Li, X. Li, X. Ma, X. Luo, *Opto-Electronic Adv.* **2023**, *6*, 230133.
[10] S. W. Moon, S. W. Moon, Y. Kim, G. Yoon, J. Rho, *Recent Progress on Ultrathin Metalenses for Flat Optics. iScience* **2020**, *23*, 101877.
[11] H. Chung, O. D. Miller, *Opt. Express* **2020**, *28*, 6945.
[12] M. Torfeh, A. Arbabi, *ACS Photonics* **2020**, *7*, 941.
[13] M. Mansouree, A. McClung, S. Samudrala, A. Arbabi, *ACS Photonics* **2021**, *8*, 455.
[14] S. Molesky, Z. Lin, A. Y. Piggott, W. Jin, J. Vuckovic, A. W. Rodriguez, *Nat. Photonics* **2018**, *12*, 659.
[15] X. Zu, X. Zu, B. Chen, N. Tang, W. E. I. Sha, J. Wang, M. Qiu, *Photonics and Nanostruct. – Fundam. Appl.* **2022**, *52*, 101075.
[16] Z. Zhao, Z. Zhao, Y. Wang, C. Guan, K. Zhang, Q. Wu, H. Li, J. Liu, S. N. Burokur, X. Ding, *PhotoniX* **2022**, *3*, 15.
[17] J. Yang, J. A. Fan, *Opt. Lett.* **2017**, *42*, 3161.
[18] C. M. Lalau-Keraly, S. Bhargava, O. D. Miller, E. Yablonovitch, *Opt. Express* **2013**, *21*, 21693.
[19] J. A. Fan, *MRS Bull.* **2020**, *45*, 196.
[20] D. Sang, M. Xu, M. Pu, F. Zhang, Y. Guo, X. Li, X. Ma, Y. Fu, X. Luo, *Laser Photonics Rev.* **2022**, *16*, 2200265.
[21] L. Dong, W. Kong, C. Wang, G. Luo, M. Pu, X. Ma, X. Li, *New J. Phys.* **2023**, *25*, 103026.
[22] Y. Zhao, M. Zhang, A. Alabastri, P. Nordlander, *ACS Nano* **2022**, *16*, 18951.
[23] J.-H. Zhang, Z. Li, J. Xu, J. Li, K. Yan, W. Cheng, M. Xin, T. Zhu, J. Du, S. Chen, X. An, Z. Zhou, L. Cheng, S. Ying, J. Zhang, X. Gao, Q. Zhang, X. Jia, Y. Shi, L. Pan, *Nat. Commun.* **2022**, *13*, 5839.
[24] S. Chen, Y. Ha, F. Zhang, M. Pu, H. Bao, M. Xu, Y. Guo, Y. Shen, X. Ma, X. Li, X. Luo, *Opto-Electronic Adv.* **2024**, *7*, 230145.
[25] R. E. Christiansen, O. Sigmund, *J. Opt. Soc. Am. B* **2021**, *38*, 496.
[26] C. F. Pan, H. Wang, H. Wang, Parvathi Nair S, Q. Ruan, S. Wredh, Y. Ke, J. Y. E. Chan, W. Zhang, C. W. Qiu, J. K. W. Yang, *Sci. Adv.* **2023**, *9*, eadj9262.
[27] A. Lohrmann, B. C. Johnson, J. C. McCallum, S. Castelletto, *Rep. Prog. Phys.* **2017**, *80*, 034502.
[28] D. Simin, D. Simin, H. Kraus, A. Sperlich, T. Ohshima, G. V. Astakhov, V. Dyakonov, *Phys. Rev. B* **2017**, *95*, 161201
[29] M. Widmann, S. Y. Lee, T. Rendler, N. T. Son, H. Fedder, S. Paik, L.-P. Yang, N. Zhao, S. Yang, I. Booker, A. Denisenko, M. Jamali, S. A. Momenzadeh, I. Gerhardt, T. Ohshima, A. Gali, E. Janzén, J. Wrachtrup, *Nat. Mater.* **2015**, *14*, 164.
[30] W. F. Koehl, B. B. Buckley, F. J. Heremans, G. Calusine, D. D. Awschalom, *Nature* **2011**, *479*, 84.
[31] O. Schaeper, Z. Yang, M. Kianinia, J. E. Fröch, A. Komar, Z. Mu, W. Gao, D. N. Neshev, I. Aharonovich, *ACS Photonics* **2022**, *9*, 1409.
[32] Y. Zheng, M. Xu, M. Pu, F. Zhang, D. Sang, Y. Guo, X. Li, X. Ma, X. Luo, *Nanophotonics* **2022**, *11*, 2967.
[33] A. S. Marathay, J. F. McCalmont, *J. Opt. Soc. Am. A Opt. Image Sci. Vis.* **2001**, *18*, 2585.
[34] J. Kennedy, R. Eberhart, presented at Proceedings of ICNN'95 - International Conference on Neural Networks, Perth, WA, Australia, August, **1995**.
[35] Xinzhong (Tom) Chen, Electromagnetic Scattering in 2D Axisymmetric Models, https://www.comsol.com/blogs/electromagnetic-scattering-in-2d-axisymmetric-models (accessed: April 2022).
[36] Z.-P. Zhuang, R. Chen, Z. B. Fan, X. N. Pang, J. W. Dong, *Nanophotonics* **2019**, *8*, 1279.
[37] X. Chen, Z. Ren, Y. Zhu, Y. Wang, J. Zhang, X. Wang, J. Xu, *SN Appl. Sci.* **2020**, *2*, 758.
[38] D. M. Lukin, M. A. Guidry, J. Vučković, *PRX Quantum* **2020**, *1*, 020102.
[39] S. Castelletto, A. Boretti, *J. Phys. Photonics* **2020**, *2*, 022001.
[40] H. Ren, J. Jang, C. Li, A. Aigner, M. Plidschun, J. Kim, J. Rho, M. A. Schmidt, S. A. Maier, *Nat. Commun.* **2022**, *13*, 4183.
[41] S. Shrestha, A. C. Overvig, M. Lu, A. Stein, N. Yu, *Light Sci Appl* **2018**, *7*, 85.
[42] Y. Wang, Q. Chen, W. Yang, Z. Ji, L. Jin, X. Ma, Q. Song, A. Boltasseva, J. Han, V. M. Shalaev, S. Xiao, *Nat. Commun.* **2021**, *12*, 5560.
[43] F. Balli, M. A. Sultan, A. Ozdemir, J. T. Hastings, *Nanophotonics* **2021**, *10*, 1259.
[44] F. Zhao, X. Jiang, S. Li, H. Chen, G. Liang, Z. Wen, Z. Zhang, G. Chen, *J. Phys. D: Appl. Phys.* **2019**, *52*, 505110.